Wall Friction and Effective Viscosity of a Homogeneous Dispersed Liquid–Liquid Flow in a Horizontal Pipe

A. Pouplin
CNRS; Fédération de recherche FERMaT FR 3089, Toulouse, France

IFP, Dept. de Mécanique Appliquée, Rueil-Malmaison, France

Université de Toulouse, INPT - UPS; Laboratoire de Génie Chimique, Toulouse, France

O. Masbernat
CNRS; Fédération de recherche FERMaT FR 3089, Toulouse, France

Université de Toulouse, INPT - UPS; Laboratoire de Génie Chimique, Toulouse, France

S. Décarre
IFP, Dept. de Mécanique Appliquée, Rueil-Malmaison, France

A. Liné
CNRS; Fédération de recherche FERMaT FR 3089, Toulouse, France

Université de Toulouse, INSA; Laboratoire d'Ingénierie des Systèmes Biologiques et des Procédés, Toulouse, France

DOI 10.1002/aic.12334
Published online July 20, 2010 in Wiley Online Library (wileyonlinelibrary.com).

Homogenous oil in water dispersion has been investigated in a horizontal pipe. The mean droplet size is 25 μm. Experiments were carried out in a 7.5-m-long transparent pipe of 50-mm internal diameter. The wall friction has been measured and modeled for a wide range of flow parameters, mixture velocities ranging from 0.28 to 1.2 m/s, and dispersed phase volume fractions up to 0.6, including turbulent, intermediate, and laminar regimes. Flow regimes have been identified from velocity profiles measured by particle image velocimetry in a matched refractive index medium. It is shown that the concept of effective viscosity is relevant to scale the friction at the wall of the dispersed flow. Based on mixture properties, the friction factor follows the Hagen-Poiseuille and the Blasius' law in laminar and turbulent regimes, respectively. Interestingly, the transition toward turbulence is delayed as the dispersed phase fraction is increased. © 2010 American Institute of Chemical Engineers *AIChE J,* 57: 1119–1131, 2011
Keywords: liquid–liquid pipe flow, homogeneous dispersed flow, PIV, effective viscosity, wall friction

Introduction

In this article, the determination of the wall friction law of a homogeneous dispersed liquid–liquid flow in a horizontal pipe is addressed. This problem is of particular interest in oil

Correspondence concerning this article should be addressed to O. Masbernat at olivier.masbernat@ensiacet.fr.

extraction processes and in many other industries dealing with the transport of emulsions.[1] Oil production is still associated with a high water throughput which tends to increase as wells are aging. There have been a number of experimental studies dealing with the flow configurations of cocurrent liquid–liquid flow in horizontal pipes. Depending on the mixture velocities and phase ratios, the flow can take different spatial configurations, dispersed or stratified, or dual-layer stratified–dispersed.[2–5] Fully dispersed flows occur at high mixture velocities, when the turbulence level is high enough to maintain a suspension of drops in the bulk flow. The flow is said to be homogeneous when the drops are uniformly distributed across the whole pipe cross section.

Homogeneous dispersed flows have given rise to quite a number of experimental studies aiming at measuring and scaling local flow field in gas–liquid, solid–liquid, and gas–particle dispersed turbulent channel flows.[6–12] Most of them deal with inertial particles or high particle Reynolds numbers (for bubbles). Detailed measurements in turbulent liquid–liquid pipe flows have been poorly addressed.[13,14]

Modeling homogeneous dispersed flows cannot be undertaken without addressing the question of turbulence damping or enhancement. An informative review of this problem can be found in the paper of Sundaresan et al.,[15] highlighting the lack of available theory to predict such mechanisms, even for dilute conditions, simple geometries, and small size particles (i.e., smaller or of the order of the Kolmogorov scale). Depending on the particle size with respect to turbulent length scales, the Stokes number (the ratio between the inclusion relaxation time and the fluid time scale ''seen'' by the inclusion), and the particle Reynolds number, the turbulence can be enhanced or reduced. The effect of concentration and polydispersity has not been achieved so far.

In the case of low inertia suspensions in liquids (i.e., low Stokes and particle Reynolds numbers), the mean slip velocity and particle inertia are negligible and it is generally accepted that the fluid–particle interaction can be described through an effective viscosity effect, which increases with increasing the concentration of the dispersed phase. This assertion is mainly based on wall friction measurements in pipe flow as a function of drop concentration.[16,17] Pal[18] observed a drag reduction effect with unstable dispersions, which disappears or is significantly reduced in the case of surfactant-stabilized emulsions. Pal also found that stabilized emulsions can be described as a single-phase flow with effective properties in both laminar and turbulent regimes. Similar results were also observed in vertical pipe flow.[17,19,20]

An interesting problem is the laminar–turbulent regime transition in dispersed flows. In the case of fine emulsions, the results of Pal[18] show that Hagen-Poiseuille law is valid for mixture Reynolds numbers ranging up to 4000, suggesting that the drops tend to delay the transition to turbulence. More recently, Matas et al.[21] studied this problem with neutrally buoyant solid particles in a pipe flow. Their results clearly show that the transition toward turbulence occurs at smaller mixture Reynolds numbers for large particle-to-pipe diameter ratios, while it is unchanged for smaller particles at concentrations lower than 0.2–0.25. Above this concentration, small particles delay the transition to turbulence. Therefore, it can be concluded that even with low inertia suspensions where effective properties can be used to scale the wall friction, laminar–turbulent transition is a function of not only the mixture Reynolds number but also of the concentration. The last observation also underlines the need for detailed flow measurements in concentrated suspension flows.

Table 1. Physical Properties of the Fluids at 29°C

Phases		Density (kg/m^3)	Viscosity (Pa s)	Refractive Index (−)	Interfacial Tension (N/m)
Dispersed	Heptane	684	4×10^{-4}	1.385	0.031
Continuous	Water–Glycerin (43% vol)	1102	3.2×10^{-3}	1.385	

In the present work, the hydrodynamic local field of a homogeneous liquid–liquid dispersion flowing in a horizontal pipe has been measured with particle image velocimetry (PIV), using the refractive index matching technique. Combining these data with pressure drop measurements, the wall friction and effective viscosity of the emulsion have been identified and scaled in a wide range of flow parameters (mixture velocity and drop concentration) from the turbulent to the laminar regime.

This article is structured as follows: In the first section, the liquid phase system, the experimental device, the measurement technique, and the flow parameters are presented. The homogeneous flow domain is drawn on a mixture velocity-concentration map and the stability of the dispersion is also addressed. The results are then presented and discussed for the three different flow regimes studied: turbulent, laminar, and intermediate. For each flow regime, the longitudinal velocity profile and the pressure drop measurement are presented and discussed at different concentrations and velocities. The effective viscosity derived from these measurements is then discussed and its evolution with concentration is compared with existing models. In the last section, the wall friction factor is presented and discussed as a function of the mixture Reynolds number. The main results are summarized in the Conclusion section.

Experimental

The experimental device and fluids used in this study are similar to those of Conan et al.[22] who studied the stratified–dispersed flow configuration. The experimental loop was modified to generate homogeneous flow of small drops using the centrifugal pump of the continuous (aqueous) loop.

Phase system

The properties of the two fluids are reported in Table 1. The continuous phase is an aqueous solution of glycerin at 43% vol/vol. The dispersed phase is *n*-heptane (technical grade) immiscible with water. At 29°C, the two phases have their refractive index matched (1.385) allowing light transmission without deviation.

Experimental setup

A schematic diagram of the whole setup is shown in Figure 1. The device comprises a 7.5-m-long horizontal pipe

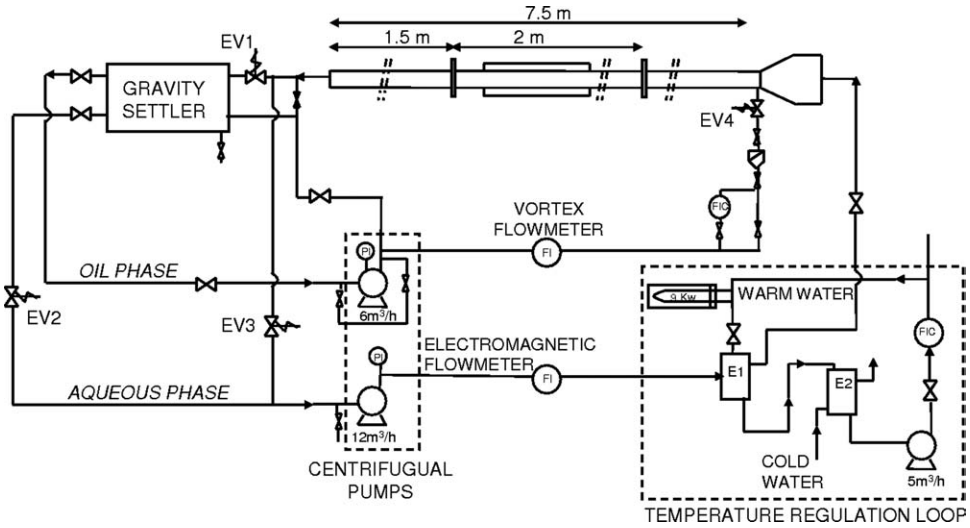

Figure 1. Schematic diagram of the two-liquid phase flow loop.

of 50-mm internal diameter, a gravity settler, an entry section, two centrifugal pumps, and a secondary loop with heat exchangers which regulate the flow temperature in the loop. To implement optical techniques, the duct is made of poly (methyl methacrylate) (PMMA), and movable square boxes (30-cm long) filled with water are mounted along the pipe to reduce optical distortions.

The two fluids are stored in the gravity settler (400 L). Each phase is pumped from the settler to the pipe inlet by centrifugal pumps of variable rotation speed. Flow rates are measured with the help of an electromagnetic flowmeter and a vortex flowmeter for the aqueous and the organic phase, respectively, with an accuracy of 0.5%. Oil and water phases merge in a Y-junction, at the pipe inlet. Upstream of the Y-junction, a convergent section has been mounted on the water loop to eliminate secondary flows in the pipe. The start-up procedure of the experimental device is operated in two stages. At first, each phase is continuously fed in the pipe and separated in the gravity settler (no dispersion is produced at this step). Then, a set of four electrovalves mounted on the circuit (see Figure 1) allow to bypass the gravity settler and direct both oil and water phases in a single circuit (the water loop) at the desired concentration. With this system, both phases flow in the aqueous phase loop and a fine dispersion of oil in water is continuously maintained by the centrifugal pump. At the end of a series of experiments, the dispersed phase fraction is measured by sedimentation of a few milliliters sample.

Flow temperature is adjusted by a heat exchanger fed by a secondary heated water circuit. The temperature of all experiments has been set to 29°C with an accuracy of 0.1°C.

Instrumentation/pressure and flow measurement systems

Pressure drop measurements were made with a differential pressure gauge. Five pressure taps were placed at 2-m intervals along the pipe. The instantaneous pressure signal was acquired at a frequency of 2 Hz and time averaged over 1-min time interval for each studied flow rate. At 2 m from the pipe inlet section, the longitudinal gradient is stable along the pipe length for both single- and two-phase flow. The uncertainty on pressure drop measurement is estimated at $\pm 11\%$.

A high speed PIV technique has been implemented to determine the two-dimensional velocity field of the aqueous phase. A vertical laser sheet illuminates a vertical median plane of the pipe. The principle of this technique consists in measuring the displacement of seeding particles between two successive images of the laser sheet separated by a constant time interval. The most probable displacement of the particles between two consecutive images is calculated from the detection of the maximum of the cross-correlation function of gray level between the two images.

Fluorescent hydrophilic microparticles were used to seed the flow. These are made of PMMA with encapsulated Rhodamine B ($\lambda = 584$ nm). Their diameter ranges between 1 and 20 μm and their density is 1.18 g/cm^3. Their Stokes number based on the terminal velocity is less than 10^{-4}. Thus, they can be considered as flow tracers over the range of flow velocity investigated. The PIV system comprises a high frequency laser (10 kHz) and a high speed camera, RS 3000 (3000 frame per second at 1024×1024 pixels^2 image resolution), equipped with a 100-mm focal lens. The laser source is a dual-head, diode-pumped Nd:YLF system ($\lambda = 527$ nm). A thin laser sheet, with a thickness less than 600 μm, is generated by a divergent lens mounted on the laser head. A 45° mirror directs the laser sheet in the vertical median plane of the pipe. The use of a high-pass filter mounted on the camera objective enables to collect only the light issued from the fluorescent microparticles ($\lambda = 584$ nm). Laser and camera are synchronized and controlled by a processor time unit. Recorded images are divided into square windows within which the gray level cross-correlation function between two consecutive images is calculated along vertical and transverse directions (using DaVis 7 software). The vector field is calculated according to a three-step iteration process with decreasing window size. The initial interrogation window is 64×64 pixels^2 and the final is 32×32 pixels^2 with a 50% overlap. This method allows a good spatial resolution of the vector field. The time between two successive images has been chosen to have a displacement of

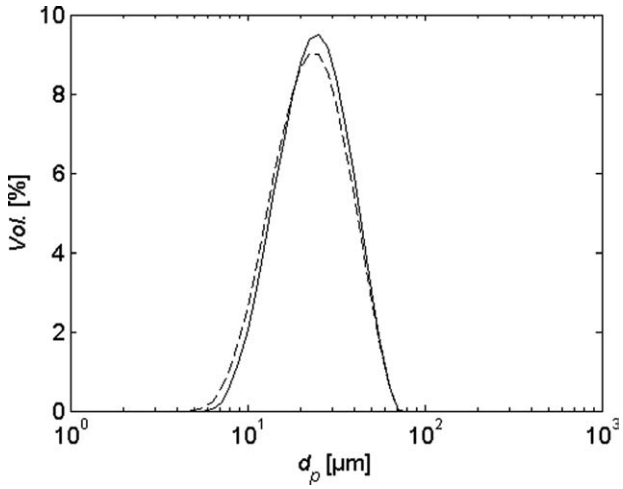

Figure 2. Drop size distribution for ϕ = 0.08 (—) and ϕ = 0.12 (- - -).

about one-fourth of the final window size. Statistical averages were performed over 2000 images corresponding to an integration time of about 4 s (acquisition frequency of 500 Hz, double pulse). Gaussian subpixel interpolation is applied to optimize the computation of the displacement, a necessary refinement for accurate measurement of low velocities near the pipe wall.[23] Image size is 1024 × 1024 pixels^2 corresponding to a field size of about 50 × 50 mm^2. The enlargement factor is estimated with a graduated transparent rule placed inside the duct. PIV measurements were realized 3.3 m after the duct entry.

Drop size

The drop size distribution was analyzed with a laser granulometer (Mastersizer 2000). A sample is directly taken from the pipe and diluted in water to increase the refractive index difference between dispersed and continuous phase. Figure 2 shows the drop size distribution for $\phi = 0.08$ and 0.12. The drop size distribution is approximately the same for both concentrations. For $0.05 < \phi < 0.25$, the mean Sauter drop diameter (d_{32}) is about 25 μm. When $\phi > 0.25$, the drop size distribution could not be measured because of the instability of the sample at high concentration. We have assumed that the mean drop size produced by the pump for higher concentration remains of the same order. The effect of the pump rotation speed was also investigated. No significant influence on drop size distribution was observed in the range of rotation speed studied ($1800 < N < 2400$ rpm). The mean diameter of the drops is smaller than the Kolmogorov length scale $(\eta = (\upsilon^3/\bar{\varepsilon})^{1/4})$ in the turbulent regime. Based on the Kolmogorov time scale, the drop Stokes number is much smaller than unity, suggesting that the effective viscosity concept is valid in such an emulsion flow. Moreover, based on the estimation of critical Capillary number and drainage time to interaction time ratio, no rupture or coalescence is expected in the pipe flow. The same drop distribution of a sample of the dispersed flow (at $\phi = 0.08$) was observed at the pipe inlet and 2 m after the pipe inlet, validating this assumption.

Flow homogeneity

A homogeneous dispersed flow is a fully dispersed flow with no mean gradient of the concentration across the pipe section. Flow homogeneity was evaluated from the radial profile of gray level in the raw images of the laser sheet. This gray level profile (averaged over 200 images) in the cross section results from the light intensity diffused by the fluorescent microparticles. Figure 3a shows the PIV raw image of a single-phase flow. On this image, white spots represent the location of the microparticles. The corresponding gray level profile is shown in Figure 3b. The vertical (radial) intensity profile is rather flat, indicating that fluorescent particles are homogeneously distributed in the aqueous phase over the cross section. The small gradient of intensity is only due to the nonhomogeneity of the laser sheet and reflections at the pipe bottom. A two-phase flow PIV raw image at high velocity ($U_m = 1.2$ m/s) appears to be identical to that of the single-phase flow (Figure 4a). Due to their small size (25 μm corresponds to less than 1 pixel), oil drops cannot be detected in

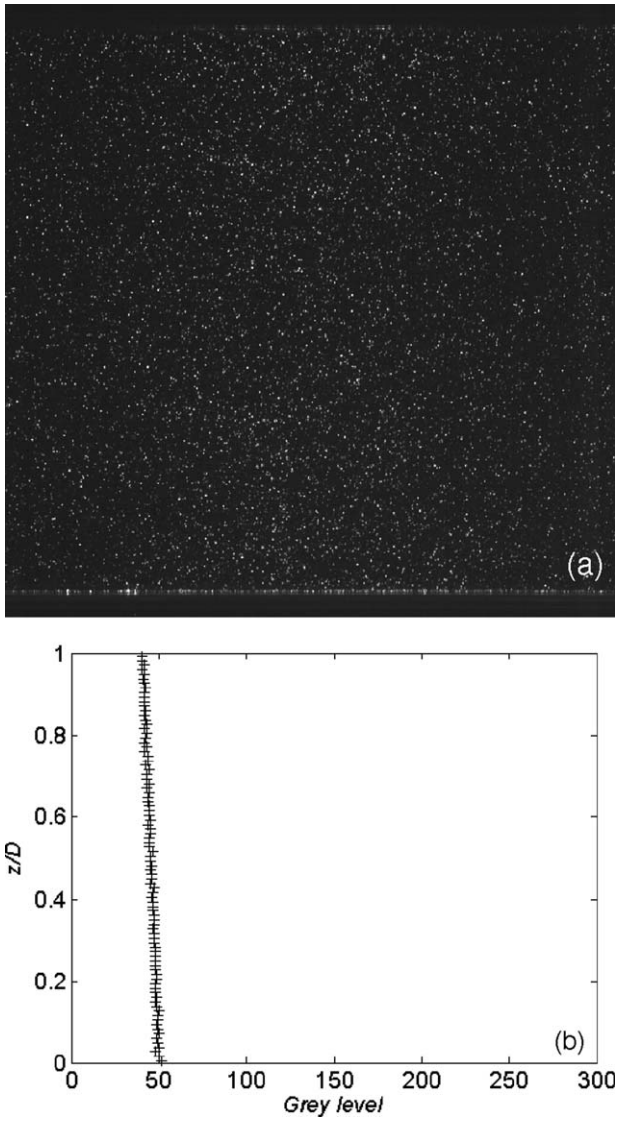

Figure 3. Single-phase flow: (a) PIV raw image, (b) vertical gray level profile (U_m = 1.2 m/s).

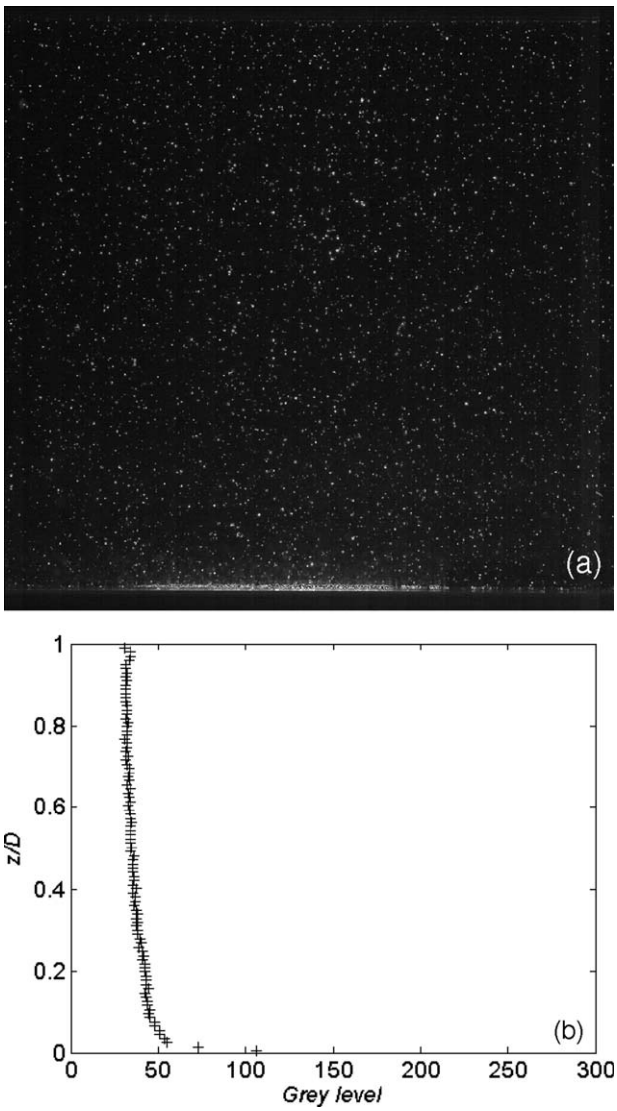

Figure 4. Homogeneous dispersed flow.

(a) PIV raw image, (b) vertical gray level profile ($\phi = 0.21$, $U_m = 1.2$ m/s).

the image. The gray level profile (Figure 4b) is practically as flat as the single-phase flow one. The dispersion can thus be considered to be homogeneous. At low velocity ($U_m = 0.28$ m/s), a layer of concentrated microparticles develops in the upper part of the wall, suggesting the occurrence of partial stratification (Figure 5a). In this case, there is an increase of gray level near the top wall (Figure 5b). This is expected to be due to the fact that, when settling in the upper part of the pipe and forming a dense layer, oil drops capture microparticles like in a flotation process. As such, a layer is free of turbulence as shown by Conan et al.[22] and the mean velocity rapidly cancels, the concentration remains stable in that layer and higher than in the bulk. Images at others velocities (not shown) indicated that the thickness of the dense layer decreases as the flow velocity increases. This layer is probably composed of the largest drops of the size distribution.

Experiments were performed over a wide range of flow mixture velocity ($0.28 < U_m < 1.2$ m/s) and phase volume fraction ($0.08 < \phi < 0.56$). A flow pattern map of all these experiments is given in Figure 6. This map represents the transition between homogeneous and partially stratified flow. Open symbols correspond to fully dispersed flow. Full symbols represent nonhomogeneous flow, when a dense layer of oil drop appears near the upper wall. In Figure 6, the map of the different flow regimes investigated has been also reported (turbulent, intermediate, and laminar). These flow regimes have been identified at steady state by a combination of measurements of velocity field and pressure drop, both presented in the next section. We note that all flow regimes meet the condition of homogeneous flow configuration, each of them in a given range of mixture velocity and dispersed phase concentration.

If the condition for flow homogeneity could be expressed as a function of a critical Froude or Richardson number in turbulent (and to some extent in the intermediate) regime, the stability of such a flow configuration in laminar regime

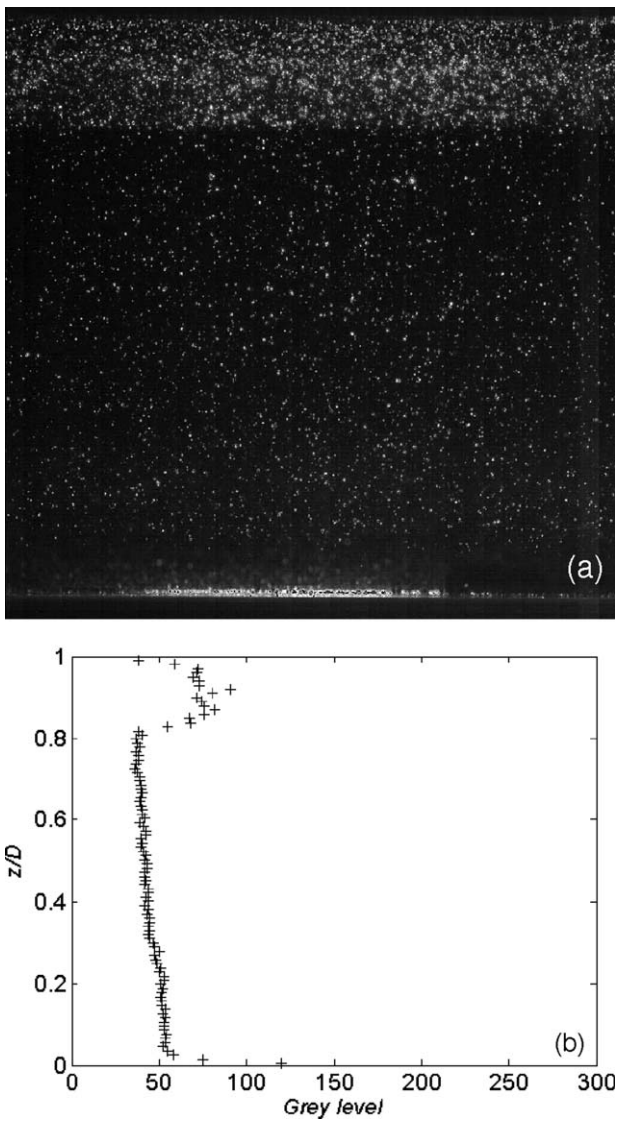

Figure 5. Partially stratified flow.

(a) PIV raw image, (b) vertical gray level profile ($\phi = 0.21$, $U_m = 0.28$ m/s).

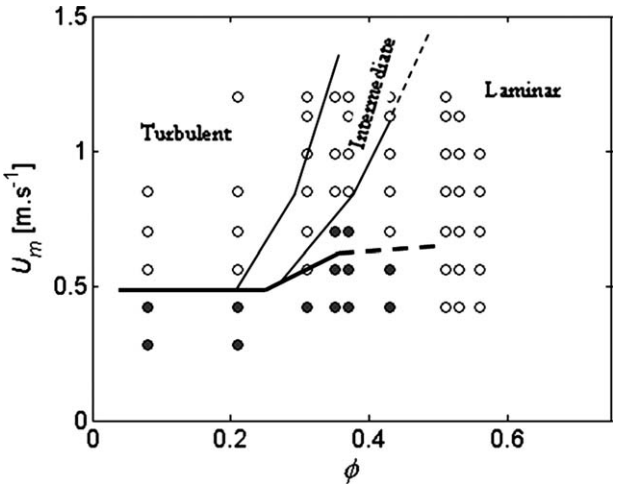

Figure 6. Flow pattern map.

(○): homogeneous flow, (●): partially stratified flow. Thin lines separate the flow regime domains. Thick line is the approximate limit between the homogeneous (above) and the partially stratified configuration (below).

is questionable. Indeed, in this regime, there are no dynamic pressure forces that prevent the drops from settling, leading to flow stratification. Shear-induced agitation is weak in the present case, especially in that range of concentration and cannot counteract the buoyancy force.[24] Therefore, the emulsion homogeneous flow is unstable in laminar regime and drops will segregate. However, based on the simple calculation of the settling velocity, it is possible to estimate the vertical displacement of the largest drops of the size distribution in the time interval between two successive passages of the flow in the pump (of the order of 16 s at 1 m/s). With a maximum drop diameter of 75 μm (see Figure 2), this displacement is of the order $D/10$. At high concentration, however, multiplying the emulsion viscosity by a factor 10 is equivalent to dividing the largest drop settling velocity and its displacement by the same factor. This is the reason why homogeneous laminar flow can be considered as stable at the scale of the present experiments.

The results for the different flow regimes are described in the next section.

Results

Turbulent regime

The velocity field PIV measurements were first performed with single-phase flow (water/glycerin mixture). For $U_0 > 0.28$ m/s ($Re_0 > 4800$), it was verified that the flow is established and parallel at 3.3 m from the pipe inlet. The longitudinal mean velocity (V_x) profile follows the expected trend in turbulent regime. An example of the radial profile of V_x is plotted in Figure 7 (cross symbols) at a mean velocity $U_0 = 0.42$ m/s ($Re_0 = 7200$). The universal power law in turbulent pipe flow reads:

$$V_x/V_{x\,max} = (1 - r/R)^{1/n} = \left(1 - 2|z/D - \frac{1}{2}|\right)^{1/n} \quad (1)$$

where $V_{x\,max}$ is the velocity at the center line and $r = |z - R|$. In Eq. 1, the exponent ($1/n$) slightly varies with the Reynolds number.[25] For $Re_0 = 7400$, $1/n$ is equal to 2/13 ($n = 6.5$) and the corresponding profile has been reported in Figure 7 (dashed line). The power law does well compared with the experimental data. By integrating (1) over the cross section, we can also compare velocity at the center line $V_{x\,max}$:

$$V_{x\,max} = U_0(1 + 1/n)(1 + 1/2n) = 0.52 \text{ m/s with } n = 13/2 \quad (2)$$

which gives a 3.3% relative difference with the experimental value (0.54 m/s).

Homogeneous turbulent two-phase flows were observed for $0.56 < U_m < 1.2$ m/s and $0.08 < \phi < 0.21$ and for $U_m > 0.85$ m/s and $\phi = 0.31$ (see flow map of Figure 6). The normalized longitudinal velocity vertical (radial) profile has been reported in Figure 7 at two concentrations ($\phi = 0.08$, $U_m = 0.56$ m/s and $\phi = 0.21$, $U_m = 0.85$ m/s). The two velocity profiles are quite symmetrical (confirming flow homogeneity) and almost identical to the single-phase flow case. Applying Eq. 2 to these profiles gives $V_{x\,max} = 0.70$ and 1.06 m/s, which are close to the experimental values (with a relative difference of 2.7 and 3.6%, respectively).

For these three cases (single-phase and the two dispersed flows), the wall law is displayed in Figure 8a, scaling the axial mean velocity by the wall friction velocity v^*, and the distance from the wall (δ) by the ratio $v^* \rho_c / \mu_c$, where μ_c and ρ_c are the continuous phase dynamic viscosity and density (i.e., at $\phi = 0$). The friction velocity is deduced from pressure drop measurements in each of these flows:

$$v^* = \sqrt{\frac{R}{2}\frac{1}{\rho_m}\left|\frac{dP}{dx}\right|} \quad (3)$$

where $\rho_m = \phi\rho_d + (1 - \phi)\rho_c$ is the mixture density of two-phase flows. In single-phase turbulent pipe flow, the velocity profile in the inertial layer is given by the universal log law:

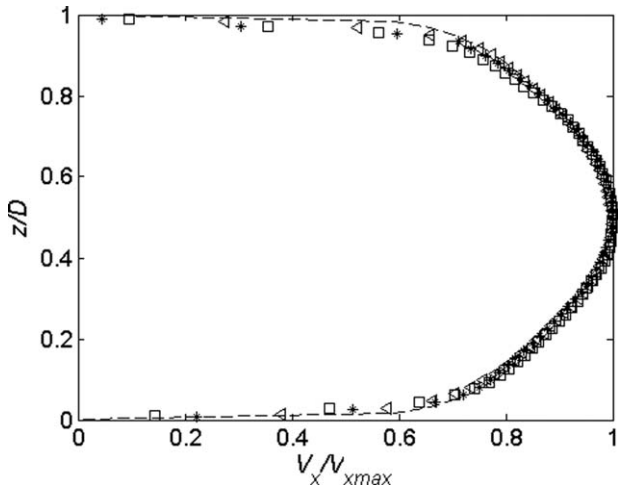

Figure 7. Normalized longitudinal velocity profile.

Single-phase flow (✱): ($U_0 = 0.42$ m/s, $Re_0 = 7200$, $V_{x\,max} = 0.54$ m/s); Two-phase flow (◁): ($\phi = 0.08$, $U_m = 0.56$ m/s, $V_{x\,max} = 0.72$ m/s), (□): ($\phi = 0.21$, $U_m = 0.85$ m/s, $V_{x\,max} = 1.1$ m/s); (- - -): $V_x/V_{x\,max} = (1 - 2|z/D - 1/2|)^{2/13}$.

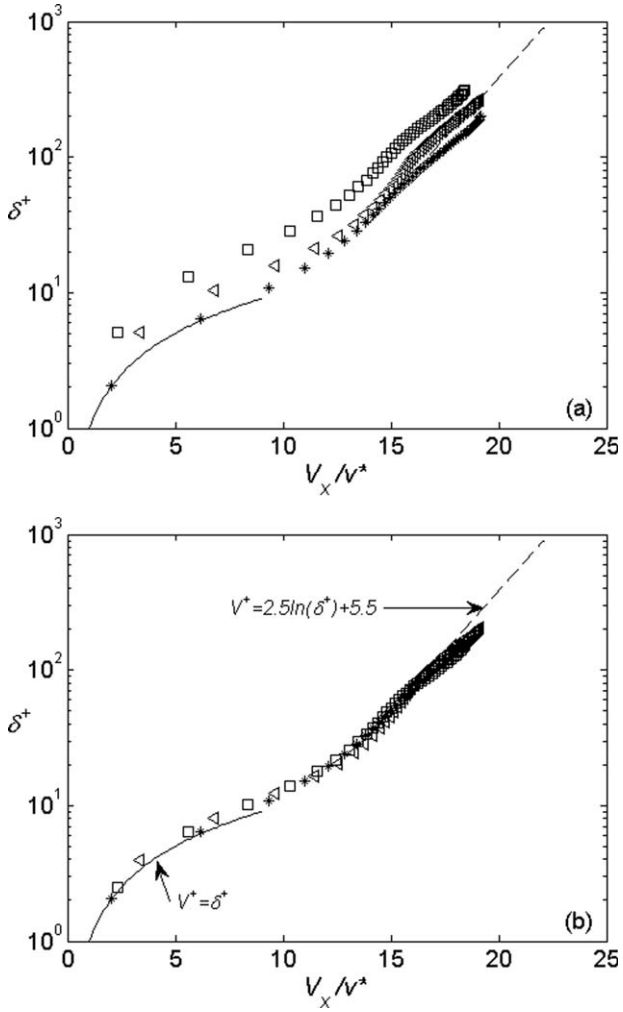

Figure 8. Wall law velocity.

Single-phase flow (✱): ($U_0 = 0.42$ m/s, $Re_0 = 7200$, $V_{x\ max} = 0.54$ m/s); Two-phase flow (◁): ($\phi = 0.08$, $U_m = 0.56$ m/s, $V_{x\ max} = 0.72$ m/s), (□): ($\phi = 0.21$, $U_m = 0.85$ m/s, $V_{x\ max} = 1.1$ m/s). (a) δ normalized by continuous phase properties, μ_c and ρ_c (b) δ normalized by mixture properties, μ_m and ρ_m.

$$\delta^+ \geq 30 \quad V^+ = \frac{1}{\kappa}\ln(\delta^+) + 5.5 \tag{4}$$

where κ is equal to 0.41, and the linear law near the wall is valid in the viscous layer:

$$0 \leq \delta^+ \leq 5 \quad V^+ = \delta^+ \tag{5}$$

with $\delta^+ = \delta\ v^*\ \rho_c/\mu_c$.

The curves of Figure 8a clearly indicate that the single-phase flow (crosses) follows the theoretical profiles in both layers up to $\delta^+ = 100$ (for larger values of δ^+, the experimental velocity data are slightly higher than the log law). In the same interval ($0 \leq \delta^+ \leq 100$), two-phase velocity profiles are shifted to the left and the shift increases with the dispersed phase concentration. Such behavior suggests an influence of the effective viscosity of the mixture. Indeed, it is possible to match the two-phase velocity profiles with that of the single phase, through a simple multiplication of each two-phase profile by a given factor. Doing so, two-phase flow data collapse on a single curve, as illustrated in Figure 8b. This multiplication amounts to replacing the continuous phase viscosity μ_c in Eqs. 4 and 5 by a mixture viscosity μ_m, equal to 4×10^{-3} Pa s with $\rho_m = 1068$ kg/m^3 for $\phi = 0.08$ and $\mu_m = 6 \times 10^{-3}$ Pa s with $\rho_m = 1014$ kg/m^3 for $\phi = 0.21$. These results show that in turbulent regime, the liquid–liquid emulsion behaves as a single fluid with mixture properties. They are also consistent with the results of Faruqui and Knudsen[19] who first used this method. According to these results, the cross-section integrated momentum balance can be applied to the mixture:

$$-\frac{dP}{dx} = f_m \frac{\rho_m U_m^2}{R} \tag{6}$$

where f_m is the mixture wall friction factor. For fully turbulent flow in smooth pipe, f_m is given by Blasius' law (in the range of Reynolds number studied ($<1210^4$), pipe roughness has no influence on wall friction factor)[26]:

$$f_m = 0.079 Re_m^{-/4} \tag{7}$$

The mixture Reynolds number is given by:

$$Re_m = \rho_m U_m D/\mu_m \tag{8}$$

where μ_m is the effective dynamic viscosity of the dispersion, a priori unknown. Therefore, the evolution of the pressure drop as a function of mean velocity reads:

$$-\frac{dP}{dx} = A \times U_m^{1.75} \quad \text{with} \quad A = \left(\frac{0.067 \rho_m^{0.75} \mu_m^{0.25}}{R_{1.25}}\right) \tag{9}$$

According to Eq. 9, the pressure gradient is proportional to the mixture velocity to the power 1.75 and the proportionality coefficient A varies as $\mu_m^{1/4}$. In Figures 9a, b, the evolution of the pressure drop as a function of the mixture velocity is reported at two concentrations, 0.08 and 0.21 in the turbulent regime. Both curves can be well fitted by a 1.75 power law, suggesting that Blasius' equation is valid. Note that on these graphs, full symbols correspond to partially stratified regime at low velocity and do not deviate much from the pressure drop law. This is due to the weak value of the stratified layer thickness δ_s. It can be shown that the main contribution to the correction of the pressure gradient is of the order of $(1 + \frac{1}{2\pi}(2\delta_s/R)^{3/2})$, which represents only a few percent in the present case, well within the range of measurement uncertainty.

For each concentration, the dynamic viscosity of the emulsion can be deduced from Eq. 9. Corresponding values are reported in Table 2. Despite the great sensitivity of the mixture viscosity to the value of A in Eq. 9 (and consequently to the pressure drop measurement uncertainty), the identified values of the effective viscosity are close to the former values derived from the matching of the log law. The values predicted by Vand's equation[27] for diluted suspensions ($\mu_m = \mu_c\ (1 + 2.5\phi + 7.35\phi^2)$) are also reported in this table. They correctly fit the values deduced from the log law. Note that the models of Manley and Mason,[28] Krieger and Dougherty,[29] or Batchelor[30] predict similar values (comparison made but not shown). It can be concluded that in

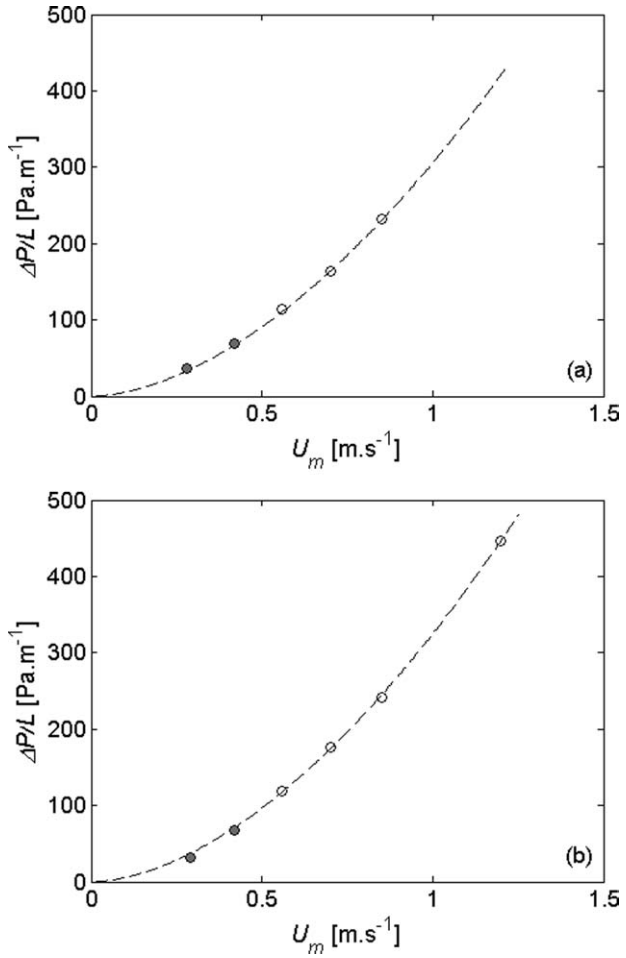

Figure 9. Evolution of the pressure drop as a function of the mixture velocity for (a) $\phi = 0.08$ and (b) $\phi = 0.21$.

Solid symbols correspond to partially homogeneous profiles. Dashed line corresponds to Eq. 9.

turbulent regime and in this range of concentration, the dispersion behaves as a suspension of noninertial hard spheres. Such behavior is consistent with the evaluation of the deformation of the drops in the turbulent flow. Based on the single-phase flow properties and the average turbulent energy dissipation rate ($\bar{\varepsilon} \cong 5.610^{-3}(U_0^3/D)$), the Kolmogorov length scale ($\eta = \left(\upsilon_c^3/\bar{\varepsilon}\right)^{1/4}$) is about 120 μm at $U_0 = 1$ m/s and is significantly larger than the drop diameter ($\sim$25 μm). The deformation seen by the drops is therefore induced by the viscous shear rate $\dot{\gamma}_k = (2\bar{\varepsilon}/15\upsilon_c)^{1/2}$. Based on that scale, the Capillary number $Ca = \mu_c\dot{\gamma}_k\bar{r}_{32}/\sigma$ is found to be the order of 10^{-4}, leading to the conclusion that the drops are not deformed.

Laminar regime

At high dispersed phase fraction $\phi \geq 0.51$ and $0.56 < U_m < 1.2$ m/s, the flow becomes laminar (see Figure 6). Two vertical profiles of the longitudinal velocity are illustrated in Figure 10 at a concentration of $\phi = 0.53$ and two mixture velocities, $U_m = 0.56$ and 0.7 m/s. These profiles are quite symmetrical. They are well fitted by the normalized parabolic profile in a tube:

$$V_x/V_{x\,max} = 1 - (r/R)^2 = 1 - 4(z/D - \frac{1}{2})^2 \quad \text{with} \quad V_{x\,max} = 2 \times U_m \tag{10}$$

The relative accuracy on the maximum velocity is 1.7 and 7% at $U_m = 0.56$ and 0.7 m/s, respectively. This result suggests that the concentrated emulsion behaves as a Newtonian fluid with an effective viscosity that can be determined using the pressure drop–mean velocity curve displayed in Figure 11. On this figure, the pressure gradient varies linearly with the mixture velocity. In this flow regime, the friction factor is therefore given by Hagen-Poiseuille law:

$$f_m = 16/Re_m \quad \text{with} \quad Re_m = \rho_m U_m D/\mu_m \tag{11}$$

And the slope is directly proportional to the effective viscosity:

$$\mu_m = \left|\frac{dP}{dx}\right| \frac{R^2}{8U_m} \tag{12}$$

The viscosity value deduced from Eq. 12 can be compared with those obtained from the velocity measured at the center line $V_{x\,max}$ (the relative difference will be the same as that between $V_{x\,max}$ and $2 \times U_m$ which is very low). For three different concentrations in the laminar regime, these values are reported in Table 3. At this concentration, the effective viscosity is an order of magnitude higher than the continuous phase viscosity (3.2×10^{-3} Pa s) and is a rapidly growing function of the concentration. Values predicted by the Eilers correlation for liquid–liquid emulsions (Eq. 17) are also reported. The correlation does fit our data very well, the discrepancy being well below the pressure drop measurement uncertainty.

As for the turbulent regime, it seems relevant to verify that the Newtonian behavior of these dispersions is consistent with a spherical shape of the drop. In laminar flow, the maximum Capillary number (based upon the mixture viscosity) can be calculated from the velocity gradient at the wall:

$$Ca_{max} = \mu_m\dot{\gamma}_{max}\bar{r}_{32}/\sigma \quad \text{with} \quad \dot{\gamma}_{max} = 4U_m/R \tag{13}$$

For a mean velocity of 1.1 m/s and an effective viscosity of 0.05 Pa s, the maximum value of the Capillary number is 3.6 $\times 10^{-3}$, suggesting that the drops remain spherical.

Note that the laminar Newtonian regime has been verified for a concentration as high as 0.56. Measurements were performed at a concentration of 70% and the velocity profiles clearly exhibited a nonNewtonian behavior (shear thinning). It is interesting to point out that Conan et al.[22] observed a similar behavior of millimeter-size dispersions (with the same phase system) for concentrations larger than 0.6. Hence, it seems

Table 2. Effective Viscosity Values Deduced From Velocity Log Law, Blasius' Law, and Vand's Equation

Concentration ϕ	0.08	0.21
(Velocity) log law [μ_m (Pa s)]	4×10^{-3}	6×10^{-3}
(Pressure drop) Blasius' law [μ_m (Pa s)]	3.7×10^{-3}	5.5×10^{-3}
Vand (1948) [μ_m (Pa s)]	4×10^{-3}	5.9×10^{-3}

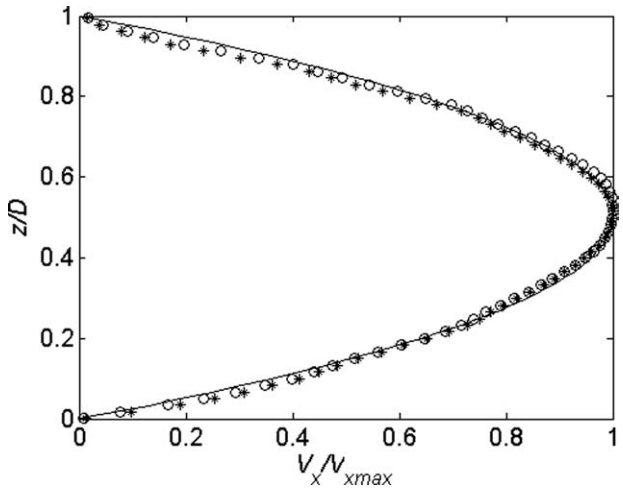

Figure 10. Normalized velocity profile at $\phi = 0.53$, (∗): $U_m = 0.56$ m/s ($V_{x\,max} = 1.1$ m/s), (○): $U_m = 0.7$ m/s ($V_{x\,max} = 1.3$ m/s), (—): parabolic profile.

reasonable to admit that, in the absence of other compounds and strong interfacial forces (the concentration of seeding microparticles is too small to have any effect on the dispersion rheology), the Newtonian behavior of non-Brownian homogeneous liquid–liquid dispersions is expected to be valid for concentrations as high as 0.55–0.6, provided that the Capillary number is small. This condition will not be fulfilled in a laminar pipe flow if the Capillary number is greater than 0.1 (which corresponds to a small finite deformation of the drop) and the Reynolds number below the critical Reynolds number ($Re_{crit} \sim 2100$ in single-phase flow), leading to a critical value of an Ohnesorge number defined as:

$$Oh = \frac{\mu_c}{\sqrt{\rho_c \sigma \overline{r_{32}}}} > Oh_{crit} = 0.31 \frac{D}{\overline{r_{32}}} \frac{g(\phi)}{\sqrt{Re_{mcrit}}} \quad \text{with} \quad g(\phi) = \frac{\rho_c}{\rho_m} \frac{\mu_c}{\mu_m} \quad (14)$$

In this relation, the function $g(\phi)$ is given by the Newtonian behavior of the emulsion. For values of the Ohnesorge number larger than this critical value, the drops will be deformed and the emulsion behavior will no longer be Newtonian. This will be the case in particular with small diameter tubes, high concentration (<0.65), and high continuous phase viscosity. Note that this range is limited by the occurrence of shear-induced drop fragmentation, occurring at critical Capillary numbers of the order of unity, for phase viscosity ratios between 10^{-2} and 10.[31] A similar calculation can be made in turbulent regime for drops size smaller than the Kolmogorov length scale, using a critical value of the Capillary number based on the viscous range shear stress and the emulsion viscosity. Using classical scaling law of fully developed turbulent pipe flow, the condition for having deformed drops in turbulent flow without breaking will be given by:

$$0.1 \frac{D}{\overline{r_{32}}} < 0.0274 \sqrt{Re_m} Ca_m < \frac{D}{\overline{r_{32}}} \quad \text{with} \quad Ca_m = \frac{\mu_m U_m}{\sigma} \quad \text{and} \quad Re_m = \frac{\rho_m U_m D}{\mu_m} \quad (15)$$

Small pipe diameter and high velocity will also favor drop deformation in that regime. As expected, the effect of the mixture viscosity is weaker than in laminar regime.

Intermediate regime

In a narrow range of mean velocity and concentration, the flow regime is neither laminar nor turbulent. This regime occurs for $0.35 < \phi < 0.45$, $0.56 < U_m < 1.2$ m/s and for $\phi = 0.31$, $U_m < 0.85$ m/s (see Figure 6). Mean velocity profiles have different shapes depending on mixture velocity and phase fraction. Two typical mean velocity profiles measured in this regime are reported in Figures 12a, b for two different concentrations at the same mean velocity ($\phi = 0.43$, $U_m = 1.2$ m/s) and ($\phi = 0.37$, $U_m = 1.2$ m/s). The mean velocity profiles of Figure 12 are clearly not symmetrical. This shape is due to the fact that the average values do not converge over a 4-s integration time scale and a much longer integration time length should be chosen in that case. This phenomenon is attributed to the alternation of laminar and turbulent flow sections at low frequency, characteristic of this intermediate regime.[25] We can observe on these graphs that the velocity profile of Figure 12a is closer to a parabolic profile while that of Figure 12b is closer to a turbulent profile, the maximal velocity being smaller in the latter case. Considering the increase of mixture viscosity with the dispersed phase concentration (due to the effective viscosity), the Reynolds number would be lower for $\phi = 0.45$ than for 0.37, which is coherent with the velocity profiles shapes. These results confirm the validity of the effective viscosity concept in the intermediate regime.

For intermediate flow regime, effective viscosities were deduced only from pressure drop measurements. The evolution of the pressure drop in the intermediate regime is characterized by a transition between a linear behavior at low velocity to a power law behavior at higher velocities, as illustrated in Figures 13a, b. There is no explicit wall friction law for intermediate regime, but the mixture viscosity can be determined with either the Hagen-Poiseuille (Eq. 11) or the Blasius (Eq. 9) law, depending on mixture velocity. For $\phi = 0.36$ (Figure 13b), pressure drop measurements are

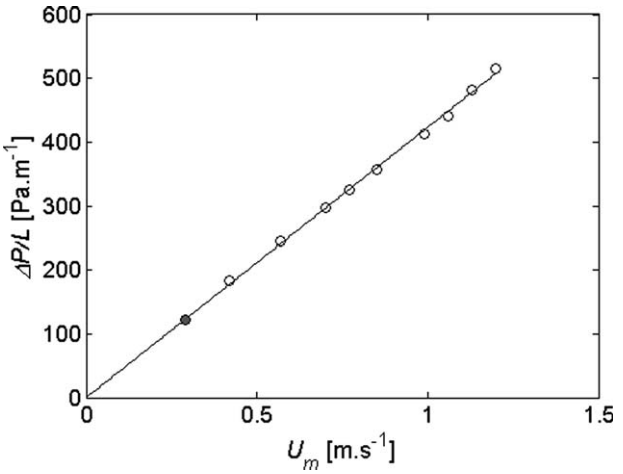

Figure 11. Evolution of the pressure drop as a function of the mixture velocity at $\phi = 0.53$.

Table 3. Effective Viscosity in Laminar Regime at High Concentration

Concentration ϕ	0.51	0.53	0.56
(Eq. 12) [μ_m (Pa s)]	0.03	0.033	0.045
(Eq. 12, $V_{x\ max}$) [μ_m (Pa s)]	0.031	0.035	0.049
Eilers (1941)	0.03	0.036	0.048

proportional to mixture velocity when $U_m < 0.7$ m/s and fit the power law $dP/dx \propto U_m^{1.75}$ when $U_m > 0.7$ m/s. For $\phi = 0.31$, only two points correspond to the linear (but also partially stratified) regime, whereas at $\phi = 0.43$ (not shown in this article), the linear regime is dominant. Viscosity values identified in that way are presented in the following section.

Mixture viscosity model

There are many effective viscosity models for low inertia suspensions and emulsions.[1,16] In the case of Newtonian emulsions, the model of Krieger and Dougherty[29] for non-Brownian monodispersed spherical particles is a reference law:

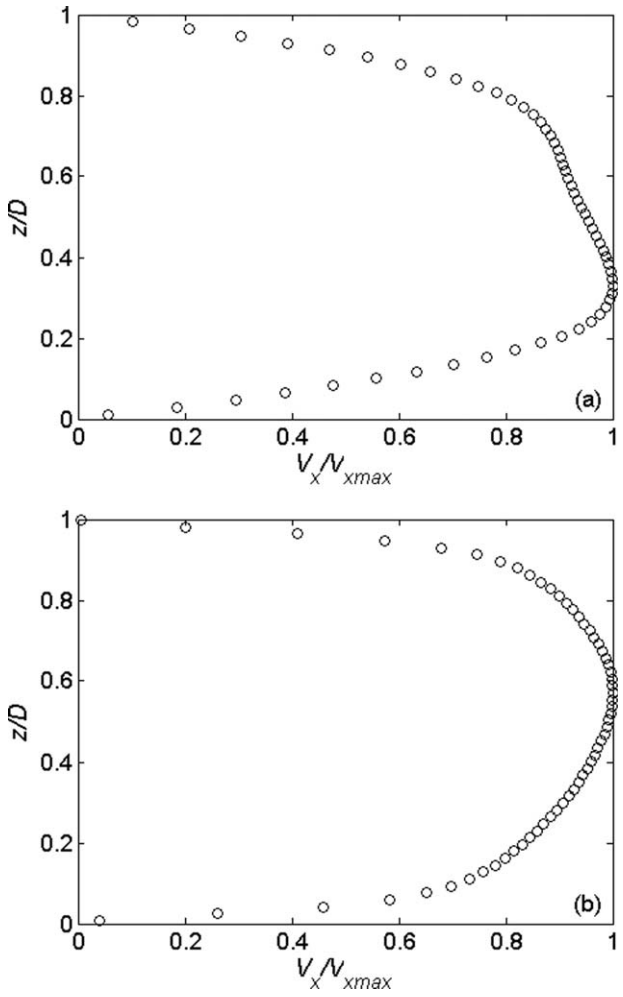

Figure 12. Axial velocity profile. (a) ϕ = 0.43, U_m = 1.2 m/s, $V_{x\ max}$ = 1.8 m/s, (b) ϕ = 0.37, U_m = 1.2 m/s, $V_{x\ max}$ = 1.6 m/s.

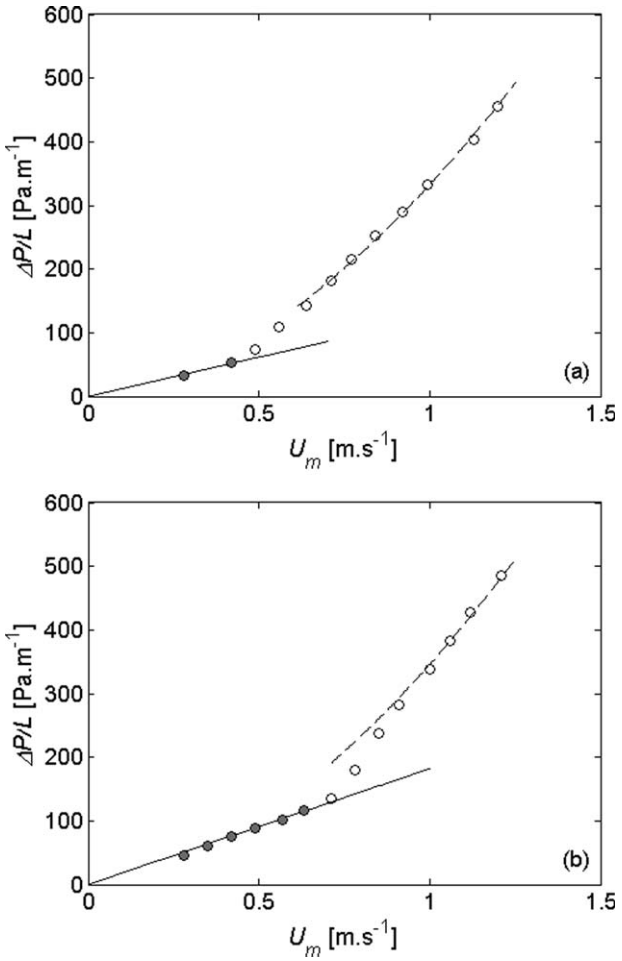

Figure 13. Pressure drop as a function of U_m (a) ϕ = 0.31, (b) ϕ = 0.36, (—): $dP/dx \propto U_m$, (- - -): $dP/dx \propto U_m^{1.75}$.

$$\mu_r = \mu_m/\mu_c = (1 - \phi/\phi_m)^{-2.5\phi_m} \tag{16}$$

where ϕ_m is the concentration at maximum packing, which is equal to 0.64 for a random packing. For polydispersed solid suspensions, ϕ_m may take larger values (0.7–0.74). In the case of a Newtonian emulsion with nondeformed drops, the internal viscosity may be accounted for Pal[32], but in most of the cases, even in the absence of surfactants, drops interfaces are immobile due to the presence of contaminants and will behave (if undeformed) as particles.[33] As a consequence, for this type of emulsion, the viscosity ratio is not expected to play a major role. The empirical model of Eilers[34] established in the case of bitumen emulsions illustrates this characteristic of a Newtonian emulsion:

$$\mu_r = \frac{\mu_m}{\mu_c} = \left(1 + \frac{2.5\phi}{2(1 - \phi/\phi_m)}\right)^2 \tag{17}$$

where ϕ_m is the maximum packing fraction of drops without deformation. In fact, the Krieger and Dougherty law and Eilers' law are very similar, they predict the mixture viscosity of Newtonian emulsion like a hard sphere suspension, with the maximum packing fraction ϕ_m being a fitting parameter

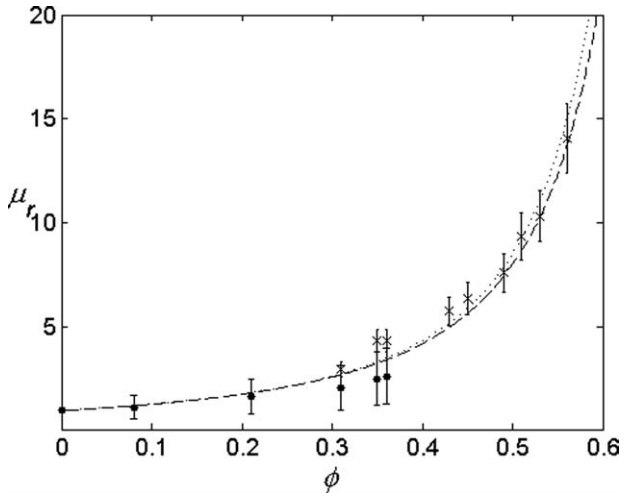

Figure 14. Relative viscosity as a function of oil volume fraction ($\phi_m = 0.74$).

(…): Eilers, (– –): Krieger and Dougherty. (●): Blasius friction factor, (×): Hagen-Poiseuille friction factor.

accounting for polydispersity. Note also that the ϕ_m value in Eqs. 16 or 17 is purely theoretical, in the sense that, for polydispersed systems (which is always the case for liquid–liquid dispersion), the Newtonian behavior will hold for concentrations ranging up to 0.55–0.65. In the intermediate region of concentrated emulsions ($0.55–0.65 < \phi < \phi_m$), Newtonian behavior is no longer valid and the apparent viscosity of the emulsion will be strongly dependent on drop mean size and mainly on size distribution. In that range of concentration, polydispersity will tend to reduce the emulsion viscosity and a strong shear-thinning behavior is observed.[35] For concentrations larger than ϕ_m (so-called highly concentrated emulsions), drop deformation will drive the emulsion rheology, whereas below the intermediate concentration range ($\phi < 0.55–0.65$), polydispersity and drop size have no effect on the effective viscosity.

Mixture viscosity values identified in the different flow regimes are plotted as a function of the concentration in Figure 14. In this graph, full symbols and crosses represent the viscosity values determined in the turbulent and laminar regimes, respectively. They are well fitted by Krieger and Dougherty and Eilers' laws with $\phi_m = 0.74$, which are nearly identical. Vertical bars represent here the maximum uncertainty related to the pressure drop and flow rate measurement ($\delta dP \approx \pm 8\%$, $\delta Q = \pm 2\%$), the relative weight effect of which is maximum in the turbulent regime. For intermediate flow regime, at $\phi = 0.31$, 0.35, and 0.36, the apparent viscosity was determined both with Hagen-Poiseuille and Blasius' laws leading to a correct framing of the viscosity models. For $\phi = 0.43$ and 0.45 when the flow tends to be laminar, the experimental values of the mixture viscosity calculated from the Hagen-Poiseuille relation are slightly underestimated by the viscosity models.

Overall, it can be concluded that Eqs. 16 and 17 give a good prediction of the effective viscosity of the flowing emulsion in all regimes, confirming the Newtonian hard sphere-type behavior of the emulsion.

Wall Friction Factor

Experimental values of wall friction calculated from Eq. 6 as a function of mixture Reynolds number using the viscosity model of Krieger and Dougherty (Eq. 16), are displayed in Figures 15a, b, and compared with the Hagen-Poiseuille and the Blasius laws. Friction factor data have been collected in the case of fully dispersed flows for Reynolds numbers ranging between 400 and 12,000, corresponding to concentration values between 0.08 and 0.56. These two extreme cases do follow well the single-phase flow friction law, the Hagen-Poiseuille law at low Re_m for $\phi = 0.56$, and the Blasius law at high Re_m for $\phi = 0.08$. When increasing the concentration between 0.08 and 0.56, as expected, the friction factor evolution with Re_m is also well predicted by these two laws.

These results confirm the early work of Baron et al.[16] in the turbulent regime, of Cengel et al.[17] and Faruqui and Knudsen[19] in the laminar and turbulent regimes, and of Pal[18] in both laminar and turbulent regimes, in the case of surfactant-stabilized emulsion of the same size range as that studied in the present work.

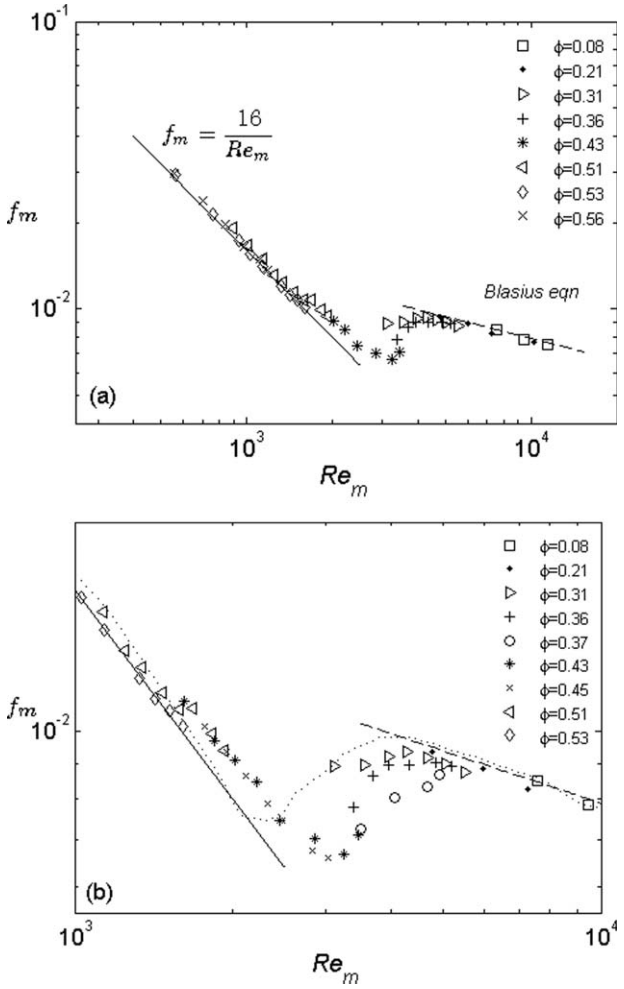

Figure 15. (a) Wall friction factor as a function of the Reynolds number, (b) Zoom of the transition region including Nikuradse experimental data (…).

However, Figure 15a exhibits some differences with single-phase flow behavior which are worth to be pointed out. These differences occur in the transition region which is shown in expanded view in Figure 15b (including additional data sets). In this graph, the dashed line represents the average curve of Nikuradse[26] data in single-phase flow. In the transition region, this curve is above our experimental data, the closest data set corresponding to it being that of $\phi = 0.31$. As the concentration is increased, experimental data move downward away from this curve, indicating a delay to transition toward fully developed turbulence. The matching of Blasius' law is observed for a Reynolds number close to 5000 at $\phi = 0.37$ and probably for a larger Reynolds number at larger concentrations, although we could not collect data in that domain, due to the insufficient pump power. Note also that the limit of Newtonian emulsion, leading to a drag reduction effect induced by the drop deformation,[18] was investigated. The evaluation of this regime through Eq. 15 indicates that the present range of flow parameters and the size distribution are far from this condition (with the phase system investigated in this study, beginning of drop deformation would be observed at a concentration of 0.56 and a Re_m of 10^4).

One can notice in Figure 15b that as the concentration is increased, the laminar–turbulent transition is delayed from $Re_m \sim 2100$ up to $Re_m \sim 3000$ for the highest two concentrations studied in that regime ($\phi = 0.43$ and 0.45). Such a result has not yet been reported for the case of a Newtonian emulsion.[18] However, focussing on the laminar–turbulence transition of neutrally buoyant coarse suspensions, Matas et al.[21] have demonstrated an influence of particle size and concentration on the critical Reynolds number. Whereas large particles tend to lower the critical mixture Reynolds number (based on the Krieger and Dougherty viscosity model), smaller particles have no effect for concentrations up to 0.25. Above this concentration, the critical Reynolds number tends to increase (although the authors could provide only a limited set of data for that range of concentration). Although no explanation was proposed by Matas et al., such behavior is consistent with the present results.

In addition to this effect of concentration in the transition domain and the increase of the critical Reynolds number, a slight deviation from the Hagen-Poiseuille friction law is observed for Reynolds numbers ranging between 1500 and 3000. In this region, the absolute value of Reynolds number exponent is slightly smaller than 1, and the coefficient slightly greater than 16, resulting in an upward shift of the friction factor compared with the $16/Re_m$ curve. One plausible explanation for this shift is the uncertainty in the pressure drop measurement and the difference between the exact value of the viscosity and that calculated by the Krieger and Dougherty model. However, the alignment on this curve over that range of Re_m of three sets of data at different concentrations (0.43, 0.45, and 0.51) suggests that this trend originates from a physical mechanism. Such a mechanism has been partially identified by the analysis of velocity field in this range of Re_m. When $Re_m < 1500$, the flow is laminar and velocity fluctuations are negligible. When $1500 < Re_m < 3000$ and $\phi \geq 0.43$, the flow is still laminar but large amplitude low-frequency fluctuations are observed and longer integration times are necessary to obtain converged parabolic profiles. These low-frequency fluctuations would explain that the slight increase of the pressure drop (which is integrated over a longer time scale) in the laminar velocity signal possibly results from the intermediate regime low-frequency fluctuations, but we have no explanation for the fact that they are not dissipated in this Reynolds range or for the effect of the concentration in the intermediate regime. It can be concluded that for a Newtonian emulsion, the critical Reynolds number increases with the concentration and the width of the mixture Reynolds range of the transition regime also increases with the concentration. Such a trend should be validated via further investigations. This problem seems to offer promising test case for numerical simulations. However, only direct numerical simulation method resolved at the scale of the drop could reproduce the effective viscosity effect (such as the force coupling method by Climent and Maxey[36]). As the particle size must be kept smaller than the Kolmogorov scale, such work seems to be out of the range of present numerical capabilities (see Sundaresan et al.[15] for a discussion on this topic).

Conclusions

Homogeneously dispersed oil in water pipe flows were studied for a wide range of flow parameters (mixture velocity and phase fraction). The dispersed phase is polydispersed with a mean drop size of about 25 μm and is stable during the measurements. Local velocity measurements have been performed at different mixture velocity and concentration, using PIV in a matched refractive index medium. The velocity fields measured for a wide range of flow regimes have shown that the emulsion behaves as a Newtonian single-phase flow in the turbulent, intermediate, and laminar regimes. The effective viscosity deduced from these velocity measurements is in agreement with the evolution of the pressure drop as a function of the mixture velocity in the different regimes. The evolution of the viscosity with the concentration of the dispersed phase can be described by both Krieger and Dougherty's and Eilers' models over the whole range of concentration ($0 < \phi < 0.56$), setting the maximum concentration to 0.74. This result validates the Newtonian behavior of the present emulsion. Using this effective viscosity, the friction factor has been plotted as a function of the mixture Reynolds number. The laminar and turbulent regime trends match Hagen-Poiseuille's and Blasius' laws, respectively. These results are in agreement with the earlier work of Baron et al.,[16] Cengel et al.,[17] Faruqui and Knudsen,[19] as well as that of Pal[18] for stabilized emulsions.

However, above a concentration of 0.31, a delay to the onset of transition is observed as the concentration is increased ($Re_{crit} \sim 3000$ for $\phi = 0.45$), as well as the width of this regime in terms of Reynolds number. Such flow behavior is in agreement with the observations of Matas et al.[21] Further experimental and/or numerical investigations are required in the transition regime to validate this trend.

Literature Cited

1. Derkach SR. Rheology of emulsion. *Adv Colloid Interface Sci.* 2009;151:1–23.
2. Arirachakaran S, Oglesby KD, Malinovski MS, Shoham O, Brill JP. *An analysis of oil/water flow phenomena in horizontal pipes.* SPE Production Operating Symp, Oklahoma, March 13–14, 1989:155–167.
3. Nädler N, Mewes D. Flow induced emulsification in the flow of two immiscible liquids in horizontal pipes. *Int J Multiphase Flow.* 1997;23:55–68.
4. Angeli P, Hewitt GF. Flow structure in horizontal oil-water flow. *Int J Multiphase Flow.* 2000;26:1117–1140.

5. Elseth G. An Experimental Study of Oil/Water Flow in Horizontal Pipes, Thesis NTNU, Norway, 2001.
6. Tsuji Y, Morikawa Y, Shiomi H. LDV measurements of an air-solid two-phase flow in a vertical pipe. *J Fluid Mech.* 1984;139:417–434.
7. Lance M, Bataille J. Turbulence in the liquid phase of a uniform bubbly air-water flow. *J Fluid Mech.* 1991;222:95–118.
8. Kulick JD, Fessler JR, Eaton JK. Particle response and turbulence modification in fully developed channel flows. *J Fluid Mech.* 1994;277:109–134.
9. Yarin LP, Hetsroni G. Turbulence intensity in dilute two-phase flows. 3. The particle-turbulence interaction in dilute two-phase flows. *Int J Multiphase Flow*. 1994;20:27–44.
10. Suzuki Y, Ikenoya M, Kasagi N. Simultaneous measurement of fluid and dispersed phases in a particle-laden turbulent channel flow with the aid of 3-D PTV. *Exp Fluids.* 2000;29(Suppl):185–193.
11. Hosokawa S, Tomiyama A. Turbulence modification in gas–liquid and solid–liquid dispersed two-phase pipe flows. *Int J Heat Fluid Flow*. 2004;25:489–498.
12. Kitagawa A, Hishida K, Kodama Y. Flow structure of microbubble-laden turbulent channel flow measured by PIV combined with the shadow image technique. *Exp Fluids*. 2005;38:466–475.
13. Kvandal HK, Elseth G, Melaaen MC. *Measurement of velocity and phase fraction in dispersed two-phase flow. Int Symp on Multiph Flow and Transport* Phenom, Antalya, Turkey, 2000:333–340.
14. Hu B, Matar OK, Hewitt GF, Angeli P. Mean and turbulent fluctuating velocities in oil-water vertical dispersed flows. *Chem Eng Sci.* 2007;62:1199–1214.
15. Sundaresan S, Eaton J, Koch DL, Ottino JM. Appendix 2: report of study group on dispersed flow. *Int J Multiphase Flow*. 2003;29: 1069–1087.
16. Baron T, Sterling CS, Schueler AP. Viscosity of suspensions-review and application to two-phase flow. *Proc Midwest Conf Fluid Mech.* 1953;3:103–128.
17. Cengel JA, Faruqui A, Finnigan JW, Wright CH, Knudsen JG. Laminar and turbulent of unstable liquid–liquid emulsions. *AIChE J*. 1962;8:335–339.
18. Pal R. Pipeline flow of unstable and surfactant-stabilized emulsions. *AIChE J*. 1993;39:1754–1764.
19. Faruqui AA, Knudsen JG. Velocity and temperature profiles of unstable liquid–liquid dispersions in vertical turbulent flow. *Chem Eng Sci*. 1962;17:897–907.
20. Ward JP, Knudsen JG. Turbulent flow of unstable liquid–liquid dispersions: drop sizes and velocity distribution. *AIChE J*. 1967;13: 356–365.
21. Matas J-P, Morris JF, Guazzelli E. Transition to turbulence in particulate pipe flow. *Phys Rev Lett*. 2003;90:1–14.
22. Conan C, Masbernat O, Décarre S, Liné A. Local hydrodynamics in a dispersed-stratified liquid–liquid pipe flow. *AIChE J*. 2007;53: 2754–2768.
23. Christensen KT. The influence of peak-locking errors on turbulence statistics computed from PIV ensembles. *Exp Fluids.* 2004;36:484–497.
24. Abbas M, Climent E, Simonin O. Fully coupled simulations of non-colloidal monodispersed sheared suspensions. *Chem Eng Res Des.* 2007;85:778–791.
25. Schlichting H, Gersten K. *Boundary Layer Theory*, 8th ed. Berlin: Springer, 2000.
26. Nikuradse J. *Laws of Flow in Rough Pipes*. Washington: NACA TM, 1950:1292.
27. Vand V. Viscosity of solutions and suspensions I. Theory. *J Phys Colloid Chem.* 1948;52:277–299.
28. Manley R, Mason SG. Particle motion in sheared suspensions. II. Collisions of uniform spheres. *J Colloid Sci*. 1952;7:354–369.
29. Krieger IM, Dougherty TJ. A mechanism for non-Newtonian flow in suspensions of rigid spheres. *Trans Soc Rheol*. 1959;III:137–152.
30. Batchelor GK. The effect of Brownian motion on the bulk stress in a suspension of spherical particles. *J Fluid Mech.* 1977;83:97–117.
31. Jansen KMB, Agterof WGM, Mellema J. Droplet breakup in concentrated emulsions. *J Rheol*. 2001;45:227–236.
32. Pal R. Novel viscosity equations for emulsions of two immiscible liquids. *J Rheol*. 2001;45:509–520.
33. Greene GA, Irvine TF, Gyves T Jr, Smith T. Drag relationships for liquid droplets settling in a continuous liquid. *AIChE J*. 1993;39: 37–41.
34. Eilers H. Die Viskosität von Emulsionen hochviskoser Stoffe als Funktion der Konzentration. *Kolloid-Z.* 1941;97:313–321.
35. Pal R. Shear viscosity behavior of emulsions of two immiscible liquids. *J Colloid Interface Sci*. 2000;225:359–366.
36. Climent E, Maxey MR. Numerical simulations of random suspensions at finite Reynolds numbers. *Int J Multiphase Flow*. 2003;29: 579–601.

Manuscript received Feb. 18, 2010, and revision received May 17, 2010.